

# High-Fidelity Antenna Pattern Modeling with Lidar Characterization

*Jeffrey J. Dumm, Michael P. Boyle, and John P. Clancy*

**A** key objective of this independent research and development (IR&D) effort was to demonstrate the capability to significantly improve antenna pattern modeling accuracy through the combined use of computer-aided design (CAD), computational electromagnetics (CEM) software, and light detection and ranging (lidar) imaging instrumentation. The method is intended for postmanufactured antennas for which CAD drawings are not available or are not sufficiently detailed; the lidar is used to reverse-engineer the shape of the antenna under test. With the advent of high-fidelity CEM computer codes, high-speed computer processors, lidar imaging instrumentation, and associated data-reduction algorithms, we have demonstrated that substantial improvements in antenna pattern modeling fidelity can be attained. We have demonstrated the process for two large reflector antennas. The method has provided computed far-field radiation patterns with a high degree of agreement with available measured data sets. In this article, we summarize the modeling methodology and the influence of reflector surface errors (the true errors and those contributed by the lidar imaging device) on antenna sidelobe levels.

## INTRODUCTION

High-fidelity pattern estimation of large reflector radar antennas is critical for many precision engagement analyses, especially in the areas of electronic attack (EA) and the suppression of enemy air defenses (SEAD). Radar-detection receiver, antiradiation homing missile

seeker, and jamming technique performance assessments are significantly influenced by the accuracy of the antenna pattern models, especially in the far-side-lobe and backlobe pattern regions. Historically, only a limited subset of the pattern data that are required for

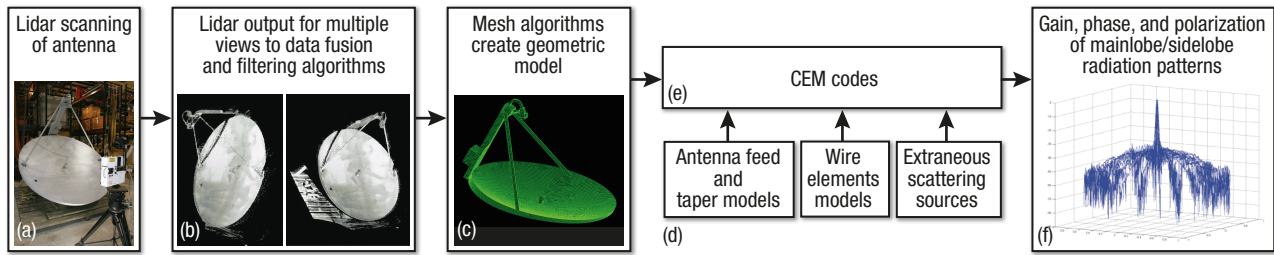


**Figure 1.** Summary of the process used to compute high-fidelity antenna patterns. A laser imaging device is used to derive the physical shape of the antenna (a); multiple images of the antenna from distinct angles are captured (b); the images are rotated and translated to a common reference frame and a CAD model of the antenna is constructed (c); models of the antenna feed structure and radiation pattern are developed (d); the feed model and the reflector model are submitted to a computational electromagnetics (CEM) code to compute the far-field radiation patterns of the antenna (e); and the complex-valued far-field patterns for each polarization basis component result (f).

sensible performance evaluations is available. These data are typically composed of single-plane cuts of azimuthal and single-plane cuts of elevation scalar gain, for a single polarization. Warfare scenarios rarely place strike and jamming aircraft flight paths along these cuts; hence, questionable antenna pattern data extrapolation or interpolation schemes must be used to complete the analyses. Furthermore, to evaluate jamming techniques against sidelobe and mainlobe threat radar electronic counter-countermeasure modes, scalar-valued gain data—for a single polarization—are insufficient; complex-valued (i.e., voltage amplitude and phase) gain data for an orthogonal polarization basis set are required.

Accurate pattern prediction in the sidelobe and backlobe regions is challenging because of the high pattern sensitivity to radar antenna structure complexities, reflector surface errors, and the scattering environment local to the radar. The objective of this project was to demonstrate the capability to significantly improve antenna pattern modeling accuracy through the combined use of recent computational software and imaging instrumentation advances.

We present data comparing predictions with measurements for an antenna used in the study. The high-fidelity modeling method was applied to a second antenna; the details of that effort are available in Refs. 1 and 2.

### Modeling Methodology

The method used to compute high-fidelity antenna patterns is depicted in Fig. 1. The antenna to be modeled is imaged using a 3-D laser scanning device such as a lidar (Fig. 1a) for the purpose of deriving the shape of the antenna. The lidar device transmits a laser beam that is directed by a servo-controlled mirror that is trained in an azimuth and elevation raster pattern. For each azimuth and elevation position, the device receives and processes the reflected laser beam and computes the range to the reflected point. The device converts the resulting polar azimuth, elevation, and range points to a point cloud of

Cartesian  $(x, y, z)$  coordinates. The scanning must be repeated for multiple lidar-to-antenna aspect angles so as to mitigate occlusion or shadowing of various features of the antenna (Fig. 1b). The set of point clouds is translated and rotated to a common reference frame to form a composite point cloud of the entire antenna. A detailed computer-aided design (CAD) model is derived from the composite point cloud (Fig. 1c). This technique provides a highly accurate physical model of the antenna. The CAD model is polygonized into a triangular mesh before being submitted to the computational electromagnetics (CEM) code.

The antenna feed illumination pattern is developed to provide a primary pattern for the reflector antenna (Fig. 1d). The far-field of the secondary (i.e., reflected)

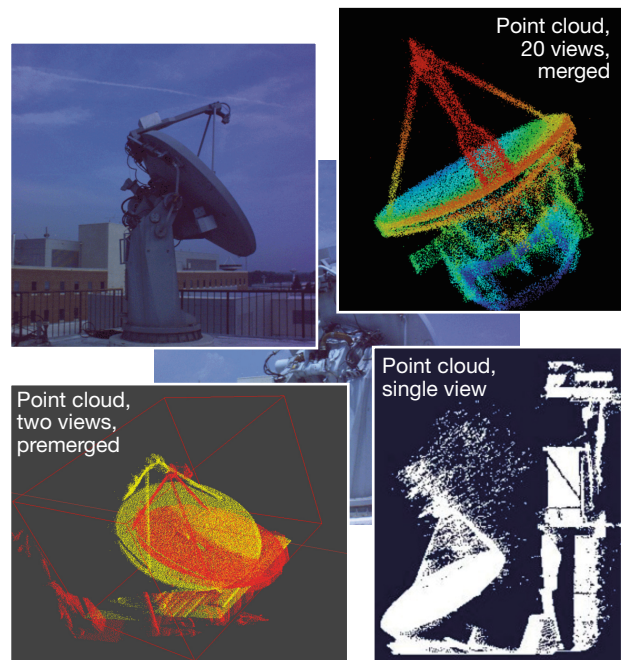


**Figure 2.** Photographs and Quick Terrain Modeler results of the alignment, merging, and extraneous point editing for 20 distinct lidar-to-antenna viewpoints of the APL SPG-62 antenna.

pattern is computed using the meshed CAD model and the primary pattern model (Figs. 1c and 1f) using an appropriate CEM code.

### Case Study

An SPG-62 antenna located at APL was used as a case study for the independent research and development (IR&D) concept. The SPG-62 antenna is a component of the U.S. Navy's MK 99 Fire Control System and is used for target illumination purposes. Photographs and lidar images of this antenna are shown in Fig. 2. Multiple lidar point clouds were collected. These data sets were aligned and assembled using the APL-developed Quick Terrain Modeler software.<sup>3</sup>

The CAD model construction process is shown in Figs. 3–5. The process began with the development of the reflector surface.<sup>4</sup> Using the composite point cloud of the entire antenna (Fig. 3a), the feed structure and struts were temporarily removed so that the reflector surface component could be built.

The point cloud of the reflector surface was groomed to exclude extraneous lidar points that were clearly outliers and not part of the surface (Fig. 3b). A second-order (quadric) surface was fit to the reflector surface lidar points (Fig. 3c). This method was chosen so as to estimate the antenna reflector conformity error to a paraboloid and to act as a filtering of the lidar points because it was known *a priori* that the lidar used possesses a relatively large measurement uncertainty ( $\sim 8$  mm,  $1\text{-}\sigma$ ), at

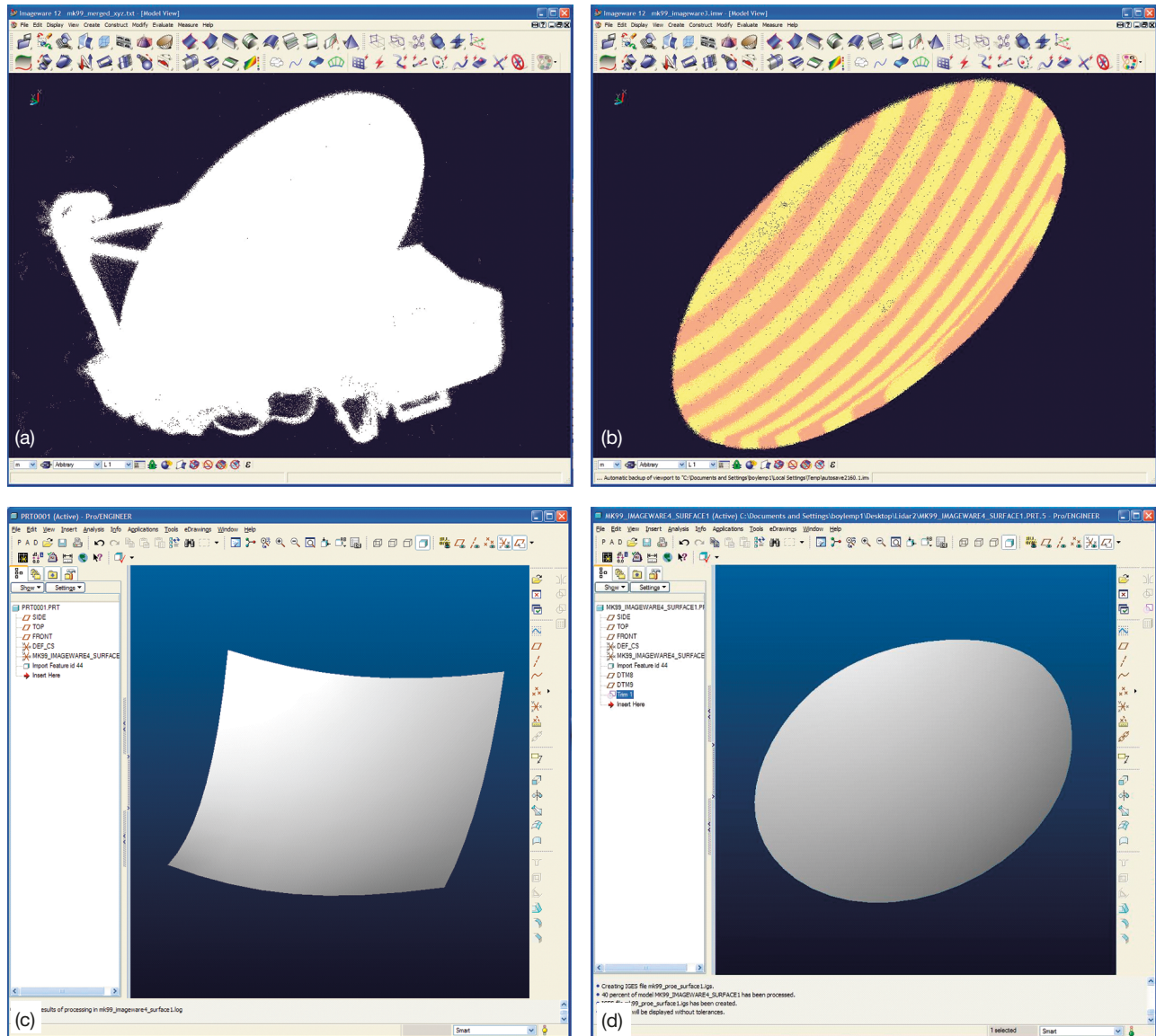


**Figure 3.** CAD model construction of SPG-62 antenna reflector surface. Composite point cloud of entire antenna (a); point cloud of reflector surface only (b); best fit of a second-order surface to reflector (c); and trimmed second-order surface for reflector rim boundary feature (d).

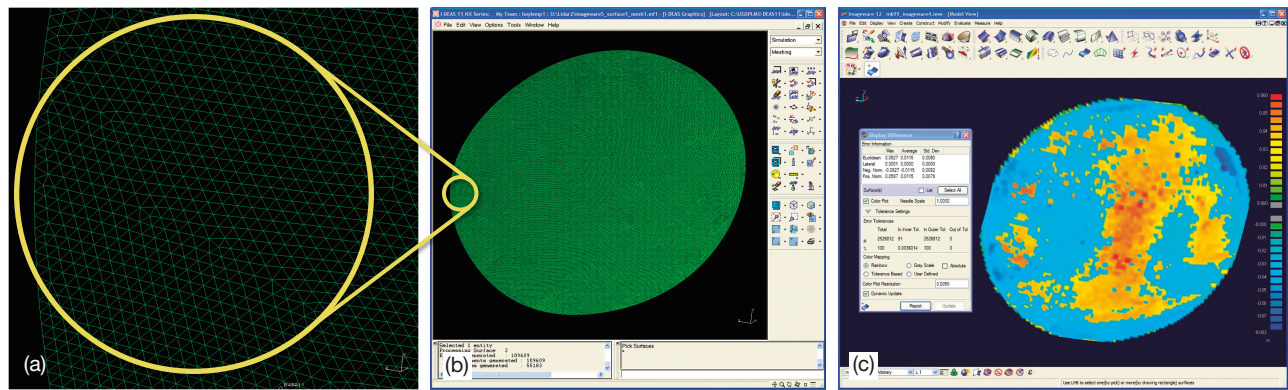


**Figure 4.** CAD model construction of SPG-62 antenna reflector surface: surface mesh and error analysis. (a) Enlarged section of a polygonized surface of a reflector model derived from a lidar point cloud. (b) Full reflector surface model. (c) Deviation of lidar points to best-fit second-order surface.

least for our purposes. In a later effort, a second antenna was modeled using a more accurate lidar.<sup>1,2</sup> Lidar instruments are available that are a few orders of magnitude more accurate than the one used for the SPG-62 imaging; however, we did not have such an instrument at our disposal at the time of this effort. The second-order fit was not strictly required; a CAD model could have been constructed from the unfiltered data directly. The rim feature was created by trimming the excess of the intersection of a plane and the second-order surface (Fig. 3d).

A meshed version of the reflector surface is shown in Figs. 4a and 4b using a triangular meshing commonly used in CAD modeling. An assessment of the differences between the point cloud and the second-order surface is shown in Fig. 4c.

The construction of the antenna CAD model was continued with the addition of the feed unit and the associated support struts. Engineering drawings of the feed were available, and hand measurements were also taken using vernier calipers. The final model is shown in Fig. 5.

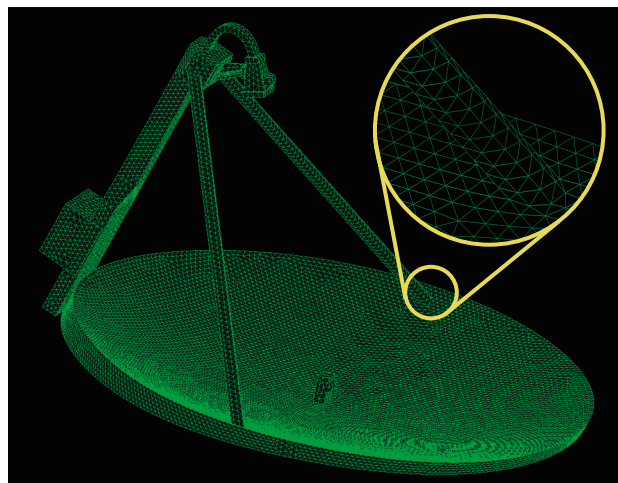


**Figure 5.** Meshed CAD model of the SPG-62 antenna derived from lidar point clouds.

### Pattern Computations

Computation of the far-field antenna patterns was conducted using the physical optics (PO) approach and also using the method of moments (MoM) approach. (See Box 1.)

#### BOX 1. COMPARISON OF THE PO APPROACH AND THE MOM APPROACH

The far-field antenna pattern is determined by the surface current density [usually denoted by a vector  $\mathbf{J}(\mathbf{x})$  with units [A/m] that exists on the antenna surface and is generated from the antenna feed.<sup>5</sup> Similarly, the radar cross section of an object is computed from the surface current, but now the surface current is induced by the incident electromagnetic wave from the radar. Once the surface current is known, the far-field representation of the vector potential is computed by taking the spatial Fourier transform of the surface current. Next, the far-field values of the electric and magnetic fields are computed from the vector potential. Finally, the far-field representations of the electric and magnetic fields determine the antenna pattern or radar cross section. The problem is reduced to knowing the surface current density, which requires an accurate description of the surface; an accurate determination of this surface was a primary objective of the project.

Once the geometry is determined, the surface current is computed. The surface current can be calculated with different approximations of varying accuracy. The first approximation is called the PO approximation and is valid when the size of the radiation object (e.g., antenna reflector) is much larger than the wavelength of the radiation and works best when the surface is a perfect conductor. (A perfect conductor is defined as a conductor where there is no electric field inside the body.) In the PO approximation, the surface current on the illuminated portion of the scattering object is given by

*Continued*

**BOX 1. COMPARISON OF THE PO APPROACH AND THE MOM APPROACH—CONTINUED**

$\vec{J}(x) = 2(\hat{n} \times \vec{H}_{inc})$ , where  $\hat{n}$  is a unit vector pointing from the scattering object to the observer and  $\vec{H}_{inc}$  is the incident magnetic field. From this expression, it is straightforward to compute the antenna pattern of a flat plate reflector antenna. That is, the incident magnetic field is modeled as a plane wave, and the resulting pattern is a product of sinc functions. For surfaces with curvature—provided that the radius of curvature of the surface features is large compared with the wavelength—the radiating object is meshed into flat facets with their individual normal vector. The problem is then basically one of bookkeeping: keeping track of which vectors are illuminated, recording the orientation of the individual unit vectors, performing the integration over each facet, and coherently summing the results.

PO approximation works well for computing the main beam properties of the antenna pattern or the specular portions of the radar cross section. By adding corrections to the surface current, the PO approximation can be modified to account for more realistic scattering processes such as diffraction (e.g., the physical theory of diffraction). However, for accurate representations of the far-sidelobe region, a more accurate technique is required, which is the MoM approach.

The MoM approach is an integral equation solution of Maxwell's equations. With the MoM approach, the reflector body is meshed into a collection of  $N$  triangles, and the surface current is expressed in terms of a known basis function defined on each facet. This discretization method results in a matrix equation for the unknown coefficients of the basis functions. The starting point for the size of the triangles is that each edge should be approximately  $\lambda/8$ , where  $\lambda$  is the wavelength of the electromagnetic radiation. However, areas of high curvature may need smaller facets, and areas with less curvature can have larger facets. The result is a matrix equation that resembles Ohm's law,  $V = I \cdot Z$ , where  $V$  is the known incident field produced by the feed,  $Z$  is called the impedance matrix, which contains the geometrical information and the integration of the Green's functions and the basis functions, and  $I$  is the surface current.

To attain the solution, one computes the inverse of the impedance matrix and multiplies it by the incident "voltage" vector. However, the impedance matrix is an  $N \times N$  matrix, so the inversion computation requires  $N^3$  computations. Next, the inverse matrix multiplies the incident field values to form the surface current. Another approach to compute the current vector is to use an iterative solver. With this technique, an initial estimate of a solution for  $I$  is made, and then iterations are conducted to find the solution that minimizes  $V - I \cdot Z$ . An iterative solver requires  $M \times N^2$  multiplications, where  $M$  is the number of iterative steps and  $N^2$  is the number of matrix multiplications of the impedance matrix and the surface current. Because the performance of the iterative solver depends on how many steps are required, there is active research on how to best condition the impedance matrix in order to reduce the number of iterations.

The main drawback to the MoM approach is that it is computationally expensive. To put this expense into perspective, it requires approximately  $10^5$  triangular facets to mesh a reflector antenna that is  $30 \lambda \times 50 \lambda$  in area and with equilateral triangles of edge length  $\lambda/8$ . Therefore, the full MoM approach would require  $10^{15}$  multiplication steps to calculate the antenna pattern for one angle, while an iterative solver would require  $10^{10}$  steps. The MoM approach is also expensive in terms of memory. The impedance matrix for this example would require  $10^{10}$  array elements, and if each element were of double complex precision, then that matrix would require approximately 100 GB of memory to store the impedance matrix values. Before it became possible to have computers with this much random access memory (RAM), these matrices were stored on the hard drive, and sophisticated "out-of-core" numerical techniques were required to solve for the surface currents. Currently, it is possible to have computers store the matrix elements in RAM. However, because the memory requirements are proportional to  $N^2$ , a reflector that was twice as large in area would require four times as much memory. It still remains a challenge to compute the radar cross section of aircraft at higher frequencies with MoM techniques. For example, the surface area of a tactical fighter aircraft is approximately  $300 \text{ m}^2$ , which would correspond to approximately  $10^9$  facets at X-band ( $\lambda = 3 \text{ cm}$ ), following the  $\lambda/8$  rule. Storing the matrix elements for this problem would require approximately  $10^8$  GB, which is not realistic for any near-term time frame.

Computation times can be decreased with a modification of the MoM algorithm called the fast multipole method (FMM). This approach uses an iterative solver and approximate expansions for the interactions between facet elements. Both the number of computational steps and the required amount of memory for the FMM approach can approach  $N \log N$ . Reducing the memory requirements improves the computational speed by allowing for more, if not all, of the impedance matrix to be stored in RAM instead of the hard drive. Both the MoM and the FMM approaches were used to compute the antenna patterns of large reflector antennas for this IR&D.

Independent of the quality of the computational algorithm, the accuracy of the solution is driven by the quality of the facet model. For example, because the MoM approach requires the inversion of a matrix, very small facets can lead to numerical problems: this can produce a row in the impedance matrix approaching zero, forming a singular matrix. Another numerical challenge exists with cavities because the wave number inside a cavity depends on the specific geometry (e.g., waveguide modes). Computational techniques will continue to improve, but the first step in any model building will always be a quality model of the geometry of the radiating object. The CEM code used to implement both the PO and the MoM methods for this effort has an efficient implementation of MoM known as the multilevel FMM (MLFMM).

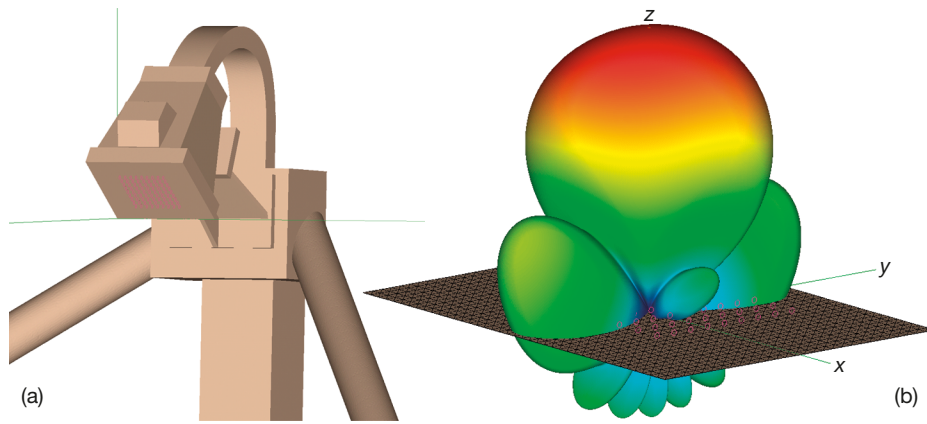


**Figure 6.** Primary pattern (i.e., feed pattern) developed for both the PO and MoM solutions. (a) Equivalent-source method located at the horn aperture. (b) Resulting radiation pattern of the horn.

A reflector antenna uses a feed structure and a reflector structure. The radiation pattern associated with the feed is referred to as the primary pattern. The primary pattern transmits onto or receives from the reflector. The net far-field pattern of the overall antenna is referred to as the secondary pattern. There is electromagnetic coupling or interaction between the feed and the reflector due to their close proximity to each other. The Lorentz reciprocity theorem can be used to describe the mutual impedance developed between the feed and the reflector and the resulting contribution to the net far-field pattern.

The feed pattern was developed by using a common technique of creating an equivalent aperture field at the mouth of the horn. This equivalent-source method used an array of magnetic current loops located at the mouth, as shown in Fig. 6a. The resulting primary pattern is shown in Fig. 6b.

The primary pattern used for the PO solution was also used for the MoM solution. Hence, the reflector illumination was identical for the two methods examined in this study. For the secondary far-field patterns using the PO method, the primary pattern was used as the illumination source without the feed struts and feed body included in the CEM model; for the MoM solution, both the feed struts and the feed body were included.

A special set of SPG-62 pattern measurements was attained in support of the IR&D effort. These measurements were an auxiliary set to those that the Navy was in the process of obtaining independent of the IR&D project. A comparison of the computed patterns versus the measured patterns is provided in Fig. 7.

Figure 7 shows the measured, the modeled PO, and the modeled MoM data sets for a single cut in the azimuthal plane. The top plot (Fig. 7a) shows the absolute gain magnitudes normalized to their respective peak values; the peak values of each data set were within a few decibels of each other. The middle plot (Fig. 7b) shows the gain differences of the modeled sets relative to

the measured data set. The bottom plot (Fig. 7c) shows the probability density function of the data for each set. The MoM solution provides a significantly better match to the measured data than the PO solution. This agreement is most notable in the far-sidelobe regions. One reason for this outcome is that the PO implementation used here did not include the feed body and feed struts in the computation of the secondary pattern. Instead, it used the primary pattern

placed at the focal point, as a point-source. Hence, no feed and strut blockage was accounted for in the PO model. The sidelobe levels of modeled data that included the blockage (MoM) are shown to be approximately 5–10 dB higher than the modeled set for which the blockage was excluded (PO). This observation suggests the importance of including the feed and strut blockage in an antenna pattern model and not necessarily a deficiency of the PO method. The full combination of the PO and MoM, with and without blockage, was not examined. However, it is well known that blockage can elevate the sidelobe levels and that the MoM has the capability to more accurately predict the low-level sidelobes than the PO method does.

### Antenna Pattern Sidelobes and Reflector Surface Roughness

A significant contributor to the sidelobe characteristics of large reflector antennas is the reflector surface conformity error (Fig. 8). This error is the deviation of the true surface shape to that intended by the designers. It is a composite of manufacturing tolerance errors, thermal strains, gravity strains, etc. Additionally, the lidar imaging instrumentation will not be perfectly accurate, and an artificial or perceived surface error component will be manifested via the instrument measurement noise. Unfortunately, it is unlikely that the true surface errors and the instrumentation-induced errors can be separated (except in simulation). Therefore, knowledge of the instrumentation error statistics is crucial, and significant image averaging may be necessary depending on the instrument precision and accuracy.

We conducted a quantitative study of the antenna pattern sidelobe sensitivity to these composite errors for both 1-D reflectors such as wires and straight tubes and also 2-D shapes such as rectangular plates (Fig. 9). Reflector antennas are commonly constructed of arrays of wires or metal tubes, as well as sections of plates.

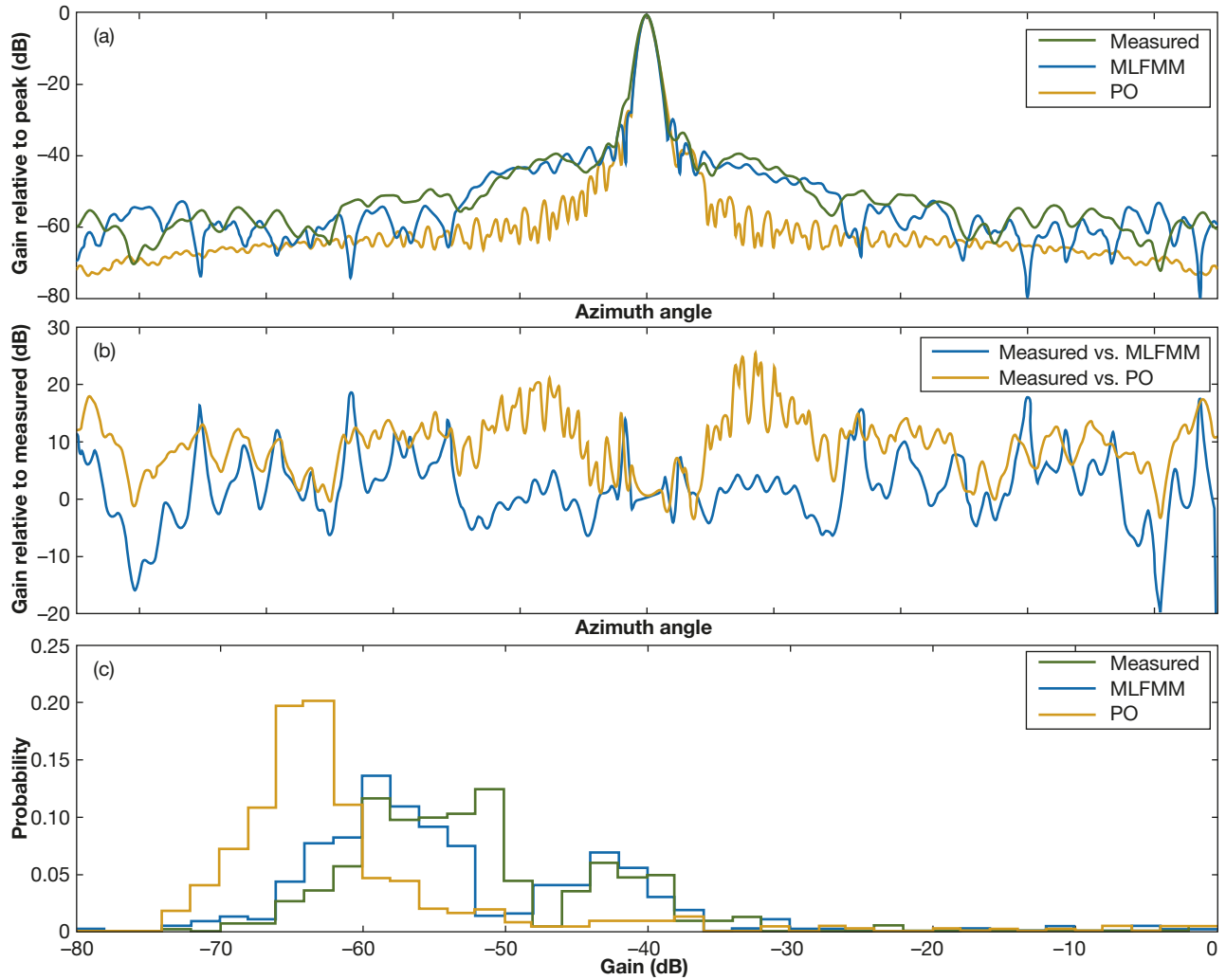


**Figure 7.** Summary of the predicted and measured antenna radiation pattern data for a single azimuthal plane cut. A comparison of the antenna patterns computed using the PO and the MoM-MLFMM methods is shown. The top plot (a) is the absolute data normalized to the peak gain. The middle plot (b) is the PO and MoM differences relative to the measured data set. The bottom plot (c) is a comparison of the probability density functions of the antenna pattern gain values for the measured, MoM-MLFMM, and PO data.

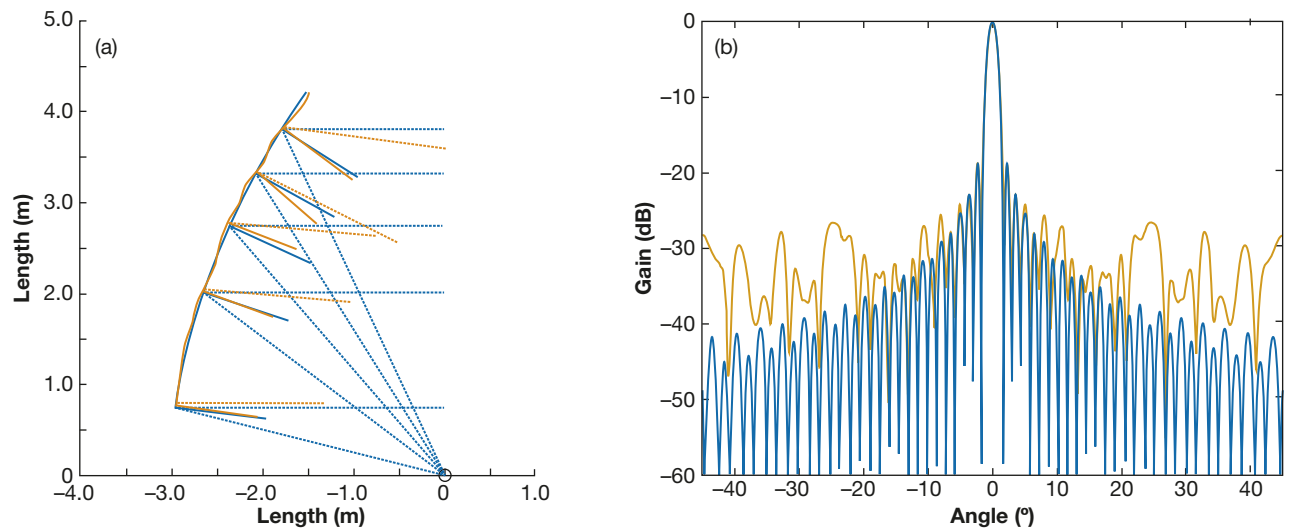


**Figure 8.** Reflector surface error and antenna radiation sidelobe degradation principle. (a) Reflector surface conformity errors produce elevated sidelobe levels in the far-field antenna radiation patterns. (b) Reflector gain pattern. Imaging instrumentation (e.g., lidar) errors contribute an artificial or perceived surface error that also elevates the computed root-mean-square (RMS) sidelobe levels. In both panels, a perfect reflector is shown in blue, and a reflector with surface errors is shown in yellow.

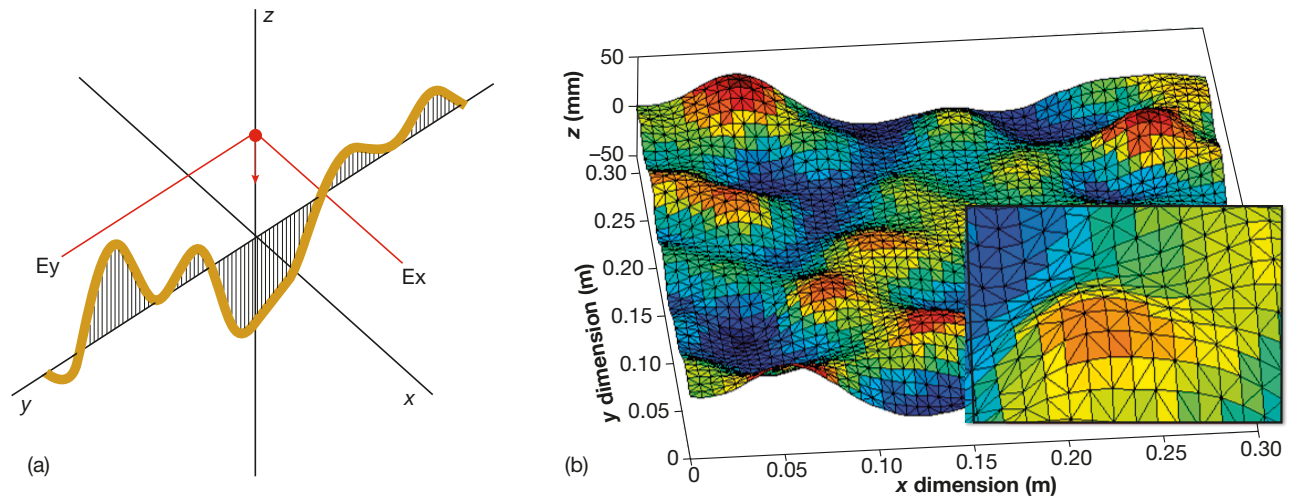


**Figure 9.** (a) A perturbed wire reflector. The wire is a perfectly conducting wire of infinitesimal diameter.  $E_x$ , x-polarized incident electric field;  $E_y$ , y-polarized incident electric field. (b) A perturbed planar sheet.

We considered the root-mean-square (RMS) surface roughness height, the spatial autocorrelation, and the spatial spectral density of the errors for likely surface height probability distributions. By way of simulation and analysis, we estimated the magnitude of sidelobe change to random perturbations to these basic reflector shapes.

There have been several studies in the past regarding the reflector sidelobe dependency on surface conformity errors; however, these studies considered only the phase perturbation of the aperture plane.<sup>6,7</sup> We investigated the effects of the integrated induced surface current in the presence of surface height errors so as to directly relate the lidar measurement precision to the far-field sidelobe degradation.<sup>5,8</sup>

Figure 10 shows an example of the far-field antenna patterns associated with the perturbed thin wire for a fixed roughness height ( $h$ ) and for several roughness correlation lengths ( $\xi$ ) as compared with the pattern for a perfectly straight wire.<sup>9</sup> As can be seen, surface errors with short correlation lengths tend to degrade a larger angular region of the radiation pattern (near and far sidelobes, and mainlobe),

whereas surface errors with long correlation lengths tend to degrade only the sidelobes near the mainbeam.

An example of a rectangular plate with surface errors is considered next. The surface shown in Fig. 11 was created using a 2-D Fourier series with uncorrelated Gaussian coefficients.<sup>10–12</sup> The induced current density for the example surface is shown in Fig. 12 superimposed onto the meshed surface. The far-field radiation pattern magnitudes produced from the integrated current density

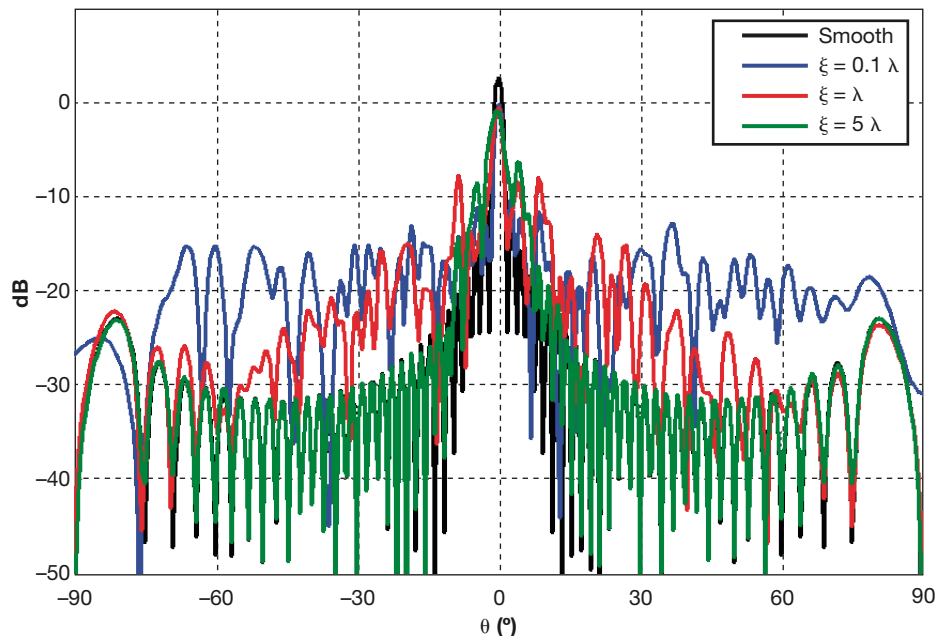


**Figure 10.** Antenna pattern of a thin,  $30\text{-}\lambda$  wire reflector with roughness ( $h = 0.05\lambda$ ) as an example of far-field pattern sensitivity to surface roughness height and correlation length. Surface conformity errors with short correlation lengths (blue) elevate a larger angular region of the sidelobes and the mainlobe; errors with long correlation lengths (green) elevate mostly the sidelobes near the mainlobe.

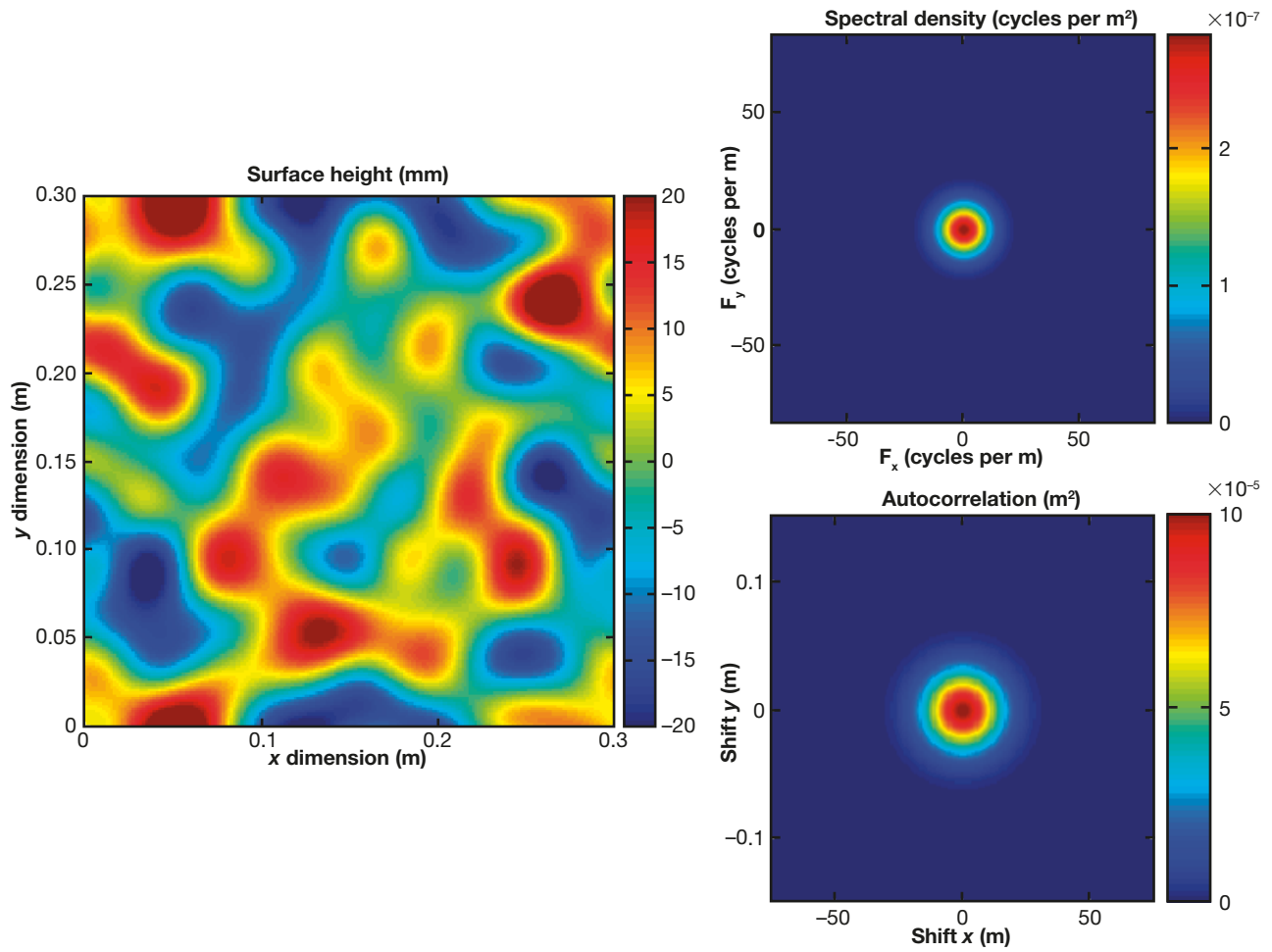


**Figure 11.** A simulated surface conformity error map for a square plate using a statistically isotropic Gaussian spatial autocorrelation function with an RMS surface height of 0.01 m and correlation length of 0.03 m.  $F_y$  and  $F_x$  are the spatial frequencies in the y and x directions, respectively.

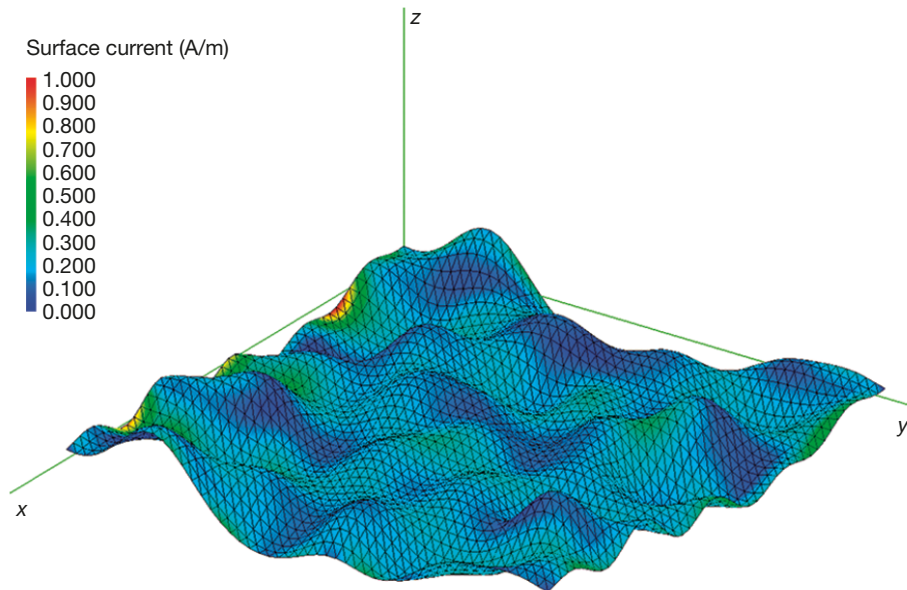


**Figure 12.** Computed current density normalized and overlaid onto a simulated rough surface. The current density subsequently is integrated as a spatial Fourier transform to produce the far-field radiation pattern.

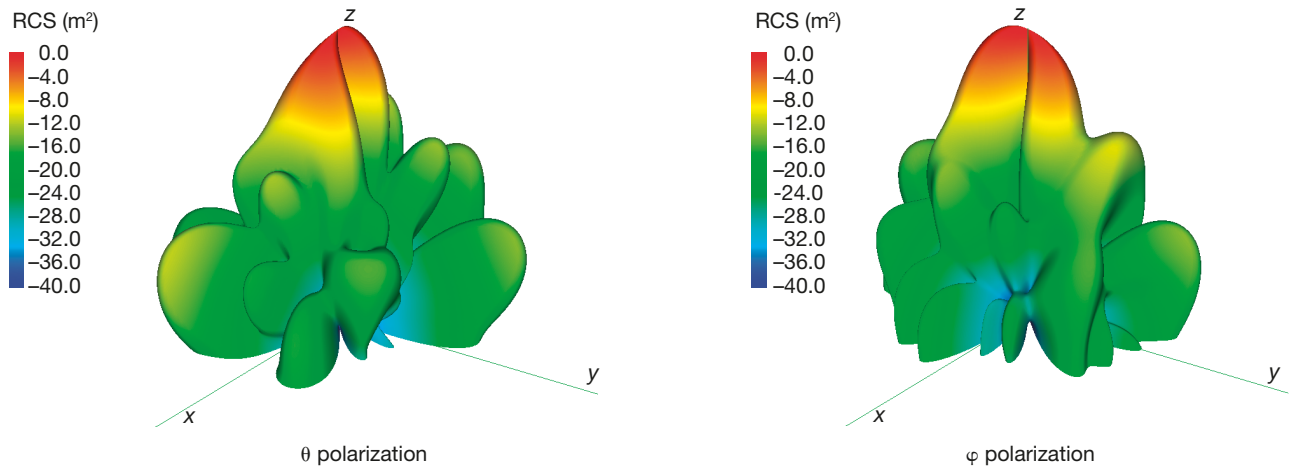


**Figure 13.** Computed far-field radiation pattern magnitude for the scattered fields in the  $\theta$ -polarized (elevation) and  $\phi$ -polarized (azimuth) directions for the rough surface considered in Fig. 12. RCS, radar cross section.

are shown in Fig. 13 for the  $\theta$ -polarized (elevation) and  $\phi$ -polarized (azimuth) scattered fields.

The PO method is a high-frequency approximation technique. This technique is only valid for “very smooth” surfaces,<sup>11</sup> that is, surfaces with radii of curvature that are large relative to the wavelength. The large radii approximate a local tangent-plane or facet model of the surface, and the far-field can be computed using simplified electromagnetic reflection coefficients that relate the incident field to the scattered field as a complex voltage ratio. The computational burden is very manageable with these techniques. The PO method is not valid for the surface error height scales that are much less than a wavelength. Our interest, for EA purposes, is primarily for reflector antennas of the surveillance-type radars such as S-band (10-cm wavelength) and the bands with even longer wavelengths. The composite surface conformity and lidar measurement RMS errors are well below 10 cm (e.g., 1 cm); hence, these reflector surfaces are considered only “slightly rough.”<sup>11</sup> Historically, slightly rough surface scattering has been done using perturbation methods. The accuracy of the PO approach under this height scale condition is subjective. Our task required us to accurately relate the surface roughness scale effects to the lidar precision requirements. We concluded that our measurement accuracy needed to be on the order of  $\lambda/30$  to  $\lambda/100$ , where  $\lambda$  is the RF wavelength.

We are able to show heuristically that sidelobe patterns for wires are more sensitive to surface height perturbations than are rectangular plates; that surface errors with short correlation lengths tend to degrade a larger angular region of the radiation pattern (i.e., both the near- and far-sidelobe regions and the main-lobe region); and that surface errors with long correlation lengths tend to degrade only the sidelobes near the mainbeam.

### An Application of a High-Fidelity Antenna Model

An application that demonstrates the need for high-fidelity antenna pattern data is multiple-loop sidelobe canceller analysis.<sup>13</sup> This issue requires pattern data in the form of complex-valued gain (i.e., amplitude and phase), for an orthogonal polarization basis set, over a sphere of compound azimuth ( $\phi$ ) and elevation ( $\theta$ ) angles. These parameters are required for all of the antennas that are used in the multiloop canceller because the interchannel amplitude, phase, and polarization properties are critical to the jamming cancellation performance. The antenna gain for a given ( $\phi$ ,  $\theta$ ) angle is commonly represented as a complex-valued two-element vector

$$\tilde{h}(\phi, \theta) = \begin{bmatrix} \tilde{h}_h(\phi, \theta) \\ \tilde{h}_v(\phi, \theta) \end{bmatrix} \text{ radar receiver antenna gain,}$$

where the first element is the horizontal polarization gain component and the second element is the vertical polarization gain component. Computation of the signal response in each channel requires knowledge of the antenna pattern vector for both the radar receiver channel and the jammer transmitter pattern for a given direction. The gain vector for the latter is

$$\tilde{g}(\phi, \theta) = \begin{bmatrix} \tilde{g}_h(\phi, \theta) \\ \tilde{g}_v(\phi, \theta) \end{bmatrix} \text{ jammer transmitter antenna gain.}$$

Typically, a sidelobe canceller system is composed of a main channel and  $N - 1$  auxiliary channels. In this  $N$ -channel system, the main channel antenna pattern has high directivity, and the remaining auxiliary channels have patterns of lower directivity.

For a scenario with  $K$  jammers versus a victim radar that uses a sidelobe canceller, the  $N$  radar receiver channel signal response can be written in vector-matrix form:

$$\tilde{\mathbf{V}}_k(t) = \begin{bmatrix} \tilde{v}_{1,k}(t) \\ \tilde{v}_{2,k}(t) \\ \tilde{v}_{3,k}(t) \\ \vdots \\ \tilde{v}_{N,k}(t) \end{bmatrix}$$

$$= \tilde{a}_k(t) \begin{bmatrix} [\tilde{g}_{k,h}\tilde{h}_{1,k,h}^* + \tilde{g}_{k,v}\tilde{h}_{1,k,v}^*] & 0 & 0 & \dots & 0 \\ 0 & [\tilde{g}_{k,h}\tilde{h}_{2,k,h}^* + \tilde{g}_{k,v}\tilde{h}_{2,k,v}^*] & 0 & \dots & 0 \\ 0 & 0 & [\tilde{g}_{k,h}\tilde{h}_{3,k,h}^* + \tilde{g}_{k,v}\tilde{h}_{3,k,v}^*] & \dots & 0 \\ \vdots & \vdots & \vdots & \ddots & \vdots \\ \vdots & \vdots & \vdots & \vdots & \vdots \\ 0 & 0 & 0 & \dots & [\tilde{g}_{k,h}\tilde{h}_{N,k,h}^* + \tilde{g}_{k,v}\tilde{h}_{N,k,v}^*] \end{bmatrix} \begin{bmatrix} e^{jk_o d_1 \sin(\theta_k)} \\ e^{jk_o d_2 \sin(\theta_k)} \\ e^{jk_o d_3 \sin(\theta_k)} \\ \vdots \\ e^{jk_o d_N \sin(\theta_k)} \end{bmatrix},$$

where  $k_o = 2\pi/\lambda =$  wave number of the  $k$ th jammer signal;  $j = \sqrt{-1}$ ;  $d_n =$  displacement of the  $n$ th canceller antenna phase center with respect to the array reference channel antenna phase center;  $d_n \sin(\theta_k) =$  approximation to  $|\mathbf{r}_k - \mathbf{r}_n|$ , the path length difference between the  $k$ th jammer and the  $n$ th channel antenna phase center;  $\mathbf{r}_k =$  position vector of the  $k$ th jammer;  $\mathbf{r}_n =$  position vector of the  $n$ th canceller channel antenna phase center; and  $\tilde{a}_k(t) =$  modulation function of the  $k$ th jammer.

Writing the above matrix equation in a more succinct form, we have:

$$\tilde{\mathbf{V}}_k(t) = \tilde{a}(t) [\tilde{g}_{k,h}\tilde{\mathbf{H}}_{k,h}^* + \tilde{g}_{k,v}\tilde{\mathbf{H}}_{k,v}^*] \tilde{\mathbf{D}}_k$$

where:

$$\tilde{\mathbf{H}}_{k,h} = \begin{bmatrix} \tilde{h}_{1,k,h} & 0 & 0 & \dots & 0 \\ 0 & \tilde{h}_{2,k,h} & 0 & \dots & 0 \\ 0 & 0 & \tilde{h}_{3,k,h} & \dots & 0 \\ \vdots & \vdots & \vdots & \ddots & \vdots \\ \vdots & \vdots & \vdots & \vdots & \vdots \\ 0 & 0 & 0 & \dots & \tilde{h}_{N,k,h} \end{bmatrix} \quad \tilde{\mathbf{H}}_{k,v} = \begin{bmatrix} \tilde{h}_{1,k,v} & 0 & 0 & \dots & 0 \\ 0 & \tilde{h}_{2,k,v} & 0 & \dots & 0 \\ 0 & 0 & \tilde{h}_{3,k,v} & \dots & 0 \\ \vdots & \vdots & \vdots & \ddots & \vdots \\ \vdots & \vdots & \vdots & \vdots & \vdots \\ 0 & 0 & 0 & \dots & \tilde{h}_{N,k,v} \end{bmatrix}$$

$$\tilde{\mathbf{D}}_k = \begin{bmatrix} e^{jk_o d_1 \sin(\theta_k)} \\ e^{jk_o d_2 \sin(\theta_k)} \\ e^{jk_o d_3 \sin(\theta_k)} \\ \vdots \\ e^{jk_o d_N \sin(\theta_k)} \end{bmatrix}.$$

The superposition of  $K$  jammer signals yields a composite array output signal vector:

$$\tilde{\mathbf{V}}(t) = \sum_{k=1}^K \tilde{\mathbf{V}}_k(t) = \sum_{k=1}^K \tilde{a}_k(t) [\tilde{g}_{k,h}\tilde{\mathbf{H}}_{k,h}^* + \tilde{g}_{k,v}\tilde{\mathbf{H}}_{k,v}^*] \tilde{\mathbf{D}}_k.$$

It is a common belief that a sidelobe canceller system can be defeated if the number of jammers in a scenario exceeds the number of canceller correlation loops. However, this is only true if the jammers are positioned so that their respective angular separations provide interchannel amplitude and phase angles in the composite channel vector,  $\tilde{\mathbf{V}}$ , that are conducive to the degradation of a useful adaptive-weight vector.<sup>14, 15</sup> The weight vector is a strong function

of the phase angles induced by the spatial vectors,  $\vec{D}_k$ , as well as the phase angles imparted by the jammer and canceller antenna complex gain products,  $\tilde{g}_k \vec{H}_{k,h}^*$  and  $\tilde{g}_k \vec{H}_{k,v}^*$ . The interchannel gain amplitude components are equally as important as the phase components in the development of the useful adaptive-weight vector.

The goal of the multijammer EA scenario is to present a signal set to the canceller system that exceeds the degrees of freedom of the correlation loops so that sufficient interchannel signal decorrelation is induced. This condition degrades, or perhaps precludes, jammer cancellation. Radar antenna sidelobe gain amplitudes and phases can be somewhat cyclic and stochastic in nature over the azimuth and elevation dimensions. Hence, it is possible to inadvertently place  $N$  jammers at angle separations that are perceived by a canceller system as being less than  $N$  jammers because of the net interchannel amplitudes and phases imparted by the radar patterns. This condition would yield effective cancellation performance for the victim radar, an undesirable outcome for the EA scenario. Knowledge of the victim radar antenna pattern complex gain values provides EA analysts with the ability to determine the optimal jammer angular separations in a scenario so that the full efficacy of the jammer suite is used for the widest compound angular region of the victim radar antenna pattern set. Interchannel signal decorrelation also occurs because of polarization mismatch between the auxiliary channels and the main channel as determined by the polarization basis components,  $\vec{H}_{k,h}$  and  $\vec{H}_{k,v}$ .

## CONCLUSIONS

We showed that a highly detailed CAD model of a large reflector antenna can be derived from lidar point-cloud images taken from multiple viewpoints, aligned, and assembled into a composite point cloud of the entire antenna. With examination of the feed design, we can develop a reasonable model of the feed primary pattern so as to compute the antenna secondary patterns using high-end CEM codes.

The fidelity of the patterns is also unprecedented for the EA community. We have demonstrated the method for two large reflector antennas, and the computed patterns showed impressive agreement with the available measured data sets. Our method yields a more complete set of patterns than any measurement effort has provided in the EA community. Our method is a full-wave solution. That is, it provides complex gain values (amplitude and phase) for an orthogonal polarization basis set, for a full sphere of observation angles, and as a function of the radar RF.

We performed analyses that relate the reflector surface roughness height and roughness correlation length to the sidelobe level degradation. If the reflector surface possesses a roughness structure with short correlation

lengths, the far-sidelobe levels are significantly elevated and the mainbeam becomes significantly deteriorated. However, if the reflector surface possesses a roughness structure with long correlation lengths, the near sidelobes are mostly elevated and the far sidelobes and mainbeam are not significantly changed relative to those provided by a perfect reflector. We determined through literature searches and our own analyses that sidelobe levels are highly sensitive to reflector surface roughness heights that are on the order of 1/30th to 1/100th of an RF wavelength,  $\lambda$ . This observation suggests that the required lidar measurement accuracy must be substantially less than these roughness height values. To this end, we have identified the most accurate coherent laser radar manufactured.<sup>16</sup> This instrument has 3-D, 2- $\sigma$  accuracies on the order of 100  $\mu\text{m}$  or less. This accuracy is an at least 80-fold improvement in accuracy relative to the lidar used in the case study and will provide measurement accuracies of  $\lambda/1000$  at S-band.

By modeling an antenna with a free-space environment assumption, the backlobe and far-sidelobe features can be predicted; extraneous scattering and propagation components can be introduced by superposition to account for site-specific conditions.

The techniques used here can be easily extended to the computation of electromagnetic scattering from arbitrarily shaped surfaces such as surface vehicles, boats, and aircraft because computation of the far-field patterns of a reflector antenna is basically a bistatic radar cross-section prediction problem.

This method of antenna pattern modeling is more cost effective and credible than traditional antenna pattern measurement methods used for the class of radars considered here. A common technique of obtaining pattern measurements is the *in situ* method using instrumented aircraft to orbit the antenna under test. Reliable cross-polarization patterns are rarely obtained with this technique because of the stringent aircraft-to-antenna geometric alignment requirements. Furthermore, atmospheric propagation modes and multipath effects lead to corrupted measured data. Modeling provides the capability to do pattern sensitivity analyses for such features as reflector surface errors or structural design modifications.

The lidar measurement technique may also be of value for radar maintenance purposes. A common problem with large reflector antennas is feed misalignment over time as a result of thermal and gravity strains. By using the lidar data of a recently aligned feed as a benchmark data set, the feed alignment can be re-measured during annual system health checks. By differencing the new alignment data set with the benchmark data set, misalignment conditions can be detected. This change-detection technique would also reveal changes to the reflector caused by aging or physical damage (bumps or distortions over time).

The laser scanning technique should also prove to be valuable as a means for collecting CAD-quality drawing data of the entire radar and transport system. These data can be archived for future documentation uses as well as for ray-trace CEM modeling.

**ACKNOWLEDGMENTS:** Key contributors to the IR&D project, in addition to the authors, were James Knight, Glenn Gealy, Myron Brown, David Grunschel, Allan Jablon, and Matthew Feinstein.

## REFERENCES

- <sup>1</sup>Dumm, J. J., Boyle, M. P., Brown, M. Z., Clancy, J. P., Gealy, G. S., and Knight, J. R., "High-Fidelity Antenna Pattern Modeling with Lidar Characterization," in *Proc. 53rd Annual Tri-Service Radar Symp.*, Orlando, FL (2007).
- <sup>2</sup>Dumm, J. J., "Test Plan for Laser Radar Characterization of Radar Asset," Technical Memorandum GVE-07-0069, JHU/APL, Laurel, MD (Aug 2007).
- <sup>3</sup>Brown, M. Z., "Data Collection and Processing for High-Fidelity Antenna Modeling," Technical Memorandum GVV-2-06S-003, JHU/APL, Laurel, MD (Sep 2006).
- <sup>4</sup>Boyle, M. P., "Reverse Engineering and Meshing of the JHU/APL MK 99 CWI X-Band Antenna," Technical Memorandum TSM-06-032, JHU/APL, Laurel, MD (Nov 2006).
- <sup>5</sup>Clancy, J. P., "Far-Field Radiation Patterns from Known Current Densities," Technical Memorandum GVA-06-0052, JHU/APL, Laurel, MD (Aug 2006).
- <sup>6</sup>Ruze, J., "Antenna Tolerance Theory – A Review," in *Proc. IEEE* **54**(4), 633–640 (1966).
- <sup>7</sup>Sinton, S., and Rahmat-Samii, Y., "Random Error Effects on Offset Cylindrical Reflector Antennas," *IEEE Trans. Antennas Propag.* **51**(6), 1331–1337 (2003).
- <sup>8</sup>Gealy, G. S., "Impact of Aperture Current Density Amplitude and Phase Errors on Antenna Pattern of a Rectangular Aperture," Technical Memorandum GVE-06-0049, JHU/APL, Laurel, MD (Aug 2006).
- <sup>9</sup>Clancy, J. P., "Far-Field Radiation Pattern of a Thin Wire Antenna," Technical Memorandum GVA-06-0053, JHU/APL, Laurel, MD (Aug 2006).
- <sup>10</sup>Rice, S. O., "Reflection of Electromagnetic Waves from Slightly Rough Surfaces," *Commun. Pure Appl. Math.* **4**, 351–378 (1951).
- <sup>11</sup>Barrick, D. E., and Peake, W. H., *Scattering from Surfaces with Different Roughness Scales: Analysis and Interpretation*, Battelle Memorial Institute Research Report, BAT-197A-10-3 (Nov 1967).
- <sup>12</sup>Dumm, J. J., "Reflector Antenna Surface Perturbation Models Using Fourier Series Techniques," Technical Memorandum GVE-07-005, JHU/APL, Laurel, MD (Jan 2007).
- <sup>13</sup>Dumm, J. J., "A Time-Domain Model of a Generic N-Loop Sidelobe Canceller," Technical Memorandum GVE-08-0065 Rev A, JHU/APL, Laurel, MD (Sept 2008).
- <sup>14</sup>Nitzberg, R., *Adaptive Signal Processing for Radar*, Artech House, Boston (1992).
- <sup>15</sup>Gealy, G. S., "General Expressions for Ideal Single-Loop Canceller Output Power and Cancellation Ratio with Multiple Jammers Present," Technical Memorandum GED-P-10-0155, JHU/APL, Laurel, MD (Dec 2010).
- <sup>16</sup>Dumm, J. J., "Recommended Coherent Laser Radar for the Purpose of Imaging Radar Antennas," Technical Memorandum GVE-07-0017, JHU/APL, Laurel, MD (Feb 2007).

# The Authors

**Jeffrey J. Dumm** is a Principal Professional Staff member in APL's Force Projection Department. He has a background in missile seeker signal processing; RF terrain scattering; adaptive signal processing; and high-fidelity modeling, simulation, and analysis of electronic attack and radar systems. **Michael P. Boyle** is a Senior Professional Staff member and Group Supervisor of the Mechanical Engineering Systems Analysis and Design Group in the Research and Exploratory Development Department (REDD). He has a background in computer-aided design, finite element analysis, and reverse engineering. **John P. Clancy** is a member of APL's Principal Professional Staff within REDD. His research interests include RF and IR signature physics, electronic warfare, and advanced technologies for improved survivability concepts. For further information on the work reported here, contact Jeffrey Dumm. His e-mail address is [jeff.dumm@jhuapl.edu](mailto:jeff.dumm@jhuapl.edu).

The Johns Hopkins APL Technical Digest can be accessed electronically at [www.jhuapl.edu/techdigest](http://www.jhuapl.edu/techdigest).